REPORT DOCUMENTATION PAGE

Form Approved
OMB No. 0704-0188

1. REPORT DATE *(DD-MM-YYYY)*	2. REPORT TYPE	3. DATES COVERED *(From - To)*
13-07-2007	Journal Article	

4. TITLE AND SUBTITLE
An experimental investigation of wave measurements using a dual-beam interferometer: Gulf Stream as a surface wave guide

5a. CONTRACT NUMBER

5b. GRANT NUMBER

5c. PROGRAM ELEMENT NUMBER
0601153N

6. AUTHOR(S)
Paul A. Hwang, Jakov V. Toporkov, Mark A. Sletten, Douglas Lamb, Dragana Perkovic

5d. PROJECT NUMBER

5e. TASK NUMBER

5f. WORK UNIT NUMBER
73-6628-06-5

7. PERFORMING ORGANIZATION NAME(S) AND ADDRESS(ES)
Naval Research Laboratory
Oceanography Division
Stennis Space Center, MS 39529-5004

8. PERFORMING ORGANIZATION REPORT NUMBER
NRL/JA/7330-06-6082

9. SPONSORING/MONITORING AGENCY NAME(S) AND ADDRESS(ES)
Office of Naval Research
800 N. Quincy St.
Arlington, VA 22217-5660

10. SPONSOR/MONITOR'S ACRONYM(S)
ONR

11. SPONSOR/MONITOR'S REPORT NUMBER(S)

12. DISTRIBUTION/AVAILABILITY STATEMENT
Approved for public release, distribution is unlimited.

13. SUPPLEMENTARY NOTES

14. ABSTRACT
A dual-beam interferometric synthetic aperture radar measures remotely two radial components of the ocean surface current from a single fight pass. Combining two passes over the same area, all three orthogonal components of the surface velocity can be retrieved. An experiment is conducted near the Gulf Stream (GS) boundary. A sharp change of the surface velocity of about 1 m/s over a 500 m lateral distance is measured. The wind and wave condition is dominated by a 14-s swell system and low wind velocity. The wave variance inside GS is about twice the wave variance outside the GS in the present data set. The difference in the wave variance is considerably higher than that can be expected from wave-current interaction. An ocean current system with strong shears such as the GS is a wave guide and can trap waves with the right combinations of wavelengths and propagation directions. Numerical calculations suggest that the wave properties of the data set may satisfy the conditions of wave trapping by the GS. The standing wave pattern on the GS side of the sharp velocity front, indicative of the long swell bouncing off the current front, also offers support for the wave guide hypothesis. In this respect, the Gulf Stream can be considered the nature's hydraulic breakwater that can attenuate about 50% of the incident wave energy generated by storms. Its role in protecting the U.S. coastlines in the Atlantic Ocean cannot be overstated.

15. SUBJECT TERMS
wave; measurement; mapping; interferometer; Gulf Stream

16. SECURITY CLASSIFICATION OF:			17. LIMITATION OF ABSTRACT	18. NUMBER OF PAGES	19a. NAME OF RESPONSIBLE PERSON
a. REPORT	b. ABSTRACT	c. THIS PAGE			Paul Hwang
Unclassified	Unclassified	Unclassified	UL	15	19b. TELEPHONE NUMBER *(include area code)* 202-767-0800

An experimental investigation of wave measurements using a dual-beam interferometer: Gulf Stream as a surface wave guide

Paul A. Hwang,[1] Jakov V. Toporkov,[1] Mark A. Sletten,[1] Douglas Lamb,[1] and Dragana Perkovic[2]

Received 9 January 2006; revised 22 May 2006; accepted 9 June 2006; published 13 September 2006.

[1] A dual-beam interferometric synthetic aperture radar measures remotely two radial components of the ocean surface current from a single flight pass. Combining two passes over the same area, all three orthogonal components of the surface velocity can be retrieved. An experiment is conducted near the Gulf Stream (GS) boundary. A sharp change of the surface velocity of about 1 m/s over a 500 m lateral distance is measured. The wind and wave condition is dominated by a 14-s swell system and low wind velocity. The wave variance inside GS is about twice the wave variance outside the GS in the present data set. The difference in the wave variance is considerably higher than that can be expected from wave-current interaction. An ocean current system with strong shears such as the GS is a wave guide and can trap waves with the right combinations of wavelengths and propagation directions. Numerical calculations suggest that the wave properties of the data set may satisfy the conditions of wave trapping by the GS. The standing wave pattern on the GS side of the sharp velocity front, indicative of the long swell bouncing off the current front, also offers support for the wave guide hypothesis. In this respect, the Gulf Stream can be considered the nature's hydraulic breakwater that can attenuate about 50% of the incident wave energy generated by storms. Its role in protecting the U.S. coastlines in the Atlantic Ocean cannot be overstated.

Citation: Hwang, P. A., J. V. Toporkov, M. A. Sletten, D. Lamb, and D. Perkovic (2006), An experimental investigation of wave measurements using a dual-beam interferometer: Gulf Stream as a surface wave guide, *J. Geophys. Res.*, *111*, C09014, doi:10.1029/2006JC003482.

1. Introduction

[2] An along-track interferometric synthetic aperture radar (InSAR) can measure the ocean surface current remotely by detecting the phase difference of the radar returns from the same surface roughness using two receiving antennas mounted on an aircraft or satellite [*Goldstein and Zebker*, 1987; *Goldstein et al.*, 1989; *Graber et al.*, 1996]. The phase difference between the received signals from the two antennas is produced by the Doppler frequency shift caused by the ocean current advecting the short surface waves that scatter the radar signals back to the receivers. To the first order of approximation, the phase shift is proportional linearly to the velocity component projected in the range direction. With proper design, the InSAR can yield sufficient spatial resolution for surface wave measurement [*Marom et al.*, 1990, 1991; *Shemer et al.*, 1993; *Goldstein et al.*, 1994]. This is a significant improvement for remote sensing of ocean waves using the SAR technology because the relationship between surface waves and the InSAR velocity product is much more straightforward than the modulation transfer function associating the surface waves and the SAR signal amplitude [e.g., *Alpers and Hasselmann*, 1978; *Hasselmann et al.*, 1985]. Because distortion of the waveform through the velocity bunching mechanism remains in the InSAR measurements, reliable retrieval of the wave information from InSAR is still limited by the nonlinearity of the wave field [e.g., *Vachon et al.*, 1999; *Bao et al.*, 1999; *He and Alpers*, 2003]. Despite this limitation, the development of InSAR is indeed a significant step forward for remote sensing of ocean waves.

[3] In the side-looking InSAR, only one radial component in the radar range direction is measured. To obtain the vector field of the ocean current, multiple non-parallel passes through the same ocean surface area have to be conducted. The concept of deriving two velocity components from the InSAR return by splitting the radar beam is discussed by *Rodriguez et al.* [1995]. *Frasier and Camps* [2001] advance the idea to employing two pairs of antennas placed with two different squint angles, one pair looking fore and one pair aft, and each pair serves as an InSAR system. The images from the two separate pairs (fore and aft) are then geo-collocated to yield the velocity vector field of the imaged ocean surface area in a single flight pass. The description of the system, called a dual-beam interferometer (DBI), has been given by *Farquharson et al.* [2004] and *Toporkov et al.* [2005], the latter paper also reports an application of the system to map out the velocity field

[1] Naval Research Laboratory, Washington, D. C., USA.
[2] Microwave Remote Sensing Laboratory, University of Massachusetts, Amherst, Massachusetts, USA.

0148-0227/06/2006JC003482$09.00

around two tidal inlets in the barrier islands west of Fort Myers, Florida. The retrieved current field follows the outflow pattern expected from the geometry of the barrier islands and the inlets. Comparisons with the tidal current magnitudes predicted by the U.S. National Ocean Service reveal discrepancies of up to 0.5 m/s. Their analyses suggest that an important factor contributing to the discrepancies is the effect of ocean surface waves to the overall InSAR velocity measurement. Numerical computations indicate that waves of a Pierson-Moskowitz spectrum for the observed wind speed (5 m/s from NEE) and the inlet geometry may have contributed to the mean Doppler frequency shifts the equivalent of −0.24 m/s in the east-west velocity component and 0.33 m/s in the north-south component.

[4] Because surface waves affect the accuracy of the surface current derivation, and that wave information is contained in the InSAR data, in this paper, we investigate the computation of surface wave spectrum using the DBI measurements. The radial velocity is contributed by all three orthogonal components of the surface current. In the 2D solution to retrieve the surface velocity from the DBI output, the vertical velocity component is assumed to be zero in the data processing [*Frasier and Camps*, 2001; *Toporkov et al.*, 2005]. In this paper, the full 3D solution to obtain all three surface velocity components by combining two flight passes is derived. In combining measurements at different times, the ergodic property of current field is assumed implicitly and the time lag is equivalent to a phase lag, thus does not change the spectral properties (Appendix A1).

[5] In the course of wave spectral analysis, it is found that for this data set (dominated by a swell system of 14-s period and low wind speed) the differences in the wave properties on the two sides of the GS velocity front is much larger than that can be explained by the current modulation of surface waves. Further analysis suggests that a more likely explanation of the observed strong enhancement of the waves inside the GS is due to wave trapping. That is, the wave properties of the data set satisfy the conditions for the GS to serve as a wave guide. This hypothesis is further supported by the conspicuous standing wave pattern (of the dominant swell length scales) observed in the GS side of the current front, indicative of the swell bouncing off the current boundary.

[6] In the following, section 2 describes the DBI current mapping experiment near the GS front east of Cape Canaveral, Florida. Section 3 presents data processing procedures and section 4 the wave spectral analysis. Section 5 discusses the wave guide hypothesis and the resolution issues, and a summary is given in section 6.

2. DBI Measurements Near the Gulf Stream Boundary

2.1. Environmental Conditions

[7] In March 2004, an experiment was conducted to test the DBI system. The general location of the experiment is offshore of Cape Canaveral, Florida (Figure 1). Two NDBC buoys (41009 and 41010) are nearby and provide the pertinent environmental information including wind velocity, air and water temperatures, and wave properties (Figure 2). Buoy 41009 is located at 28.50°N 80.17°W,

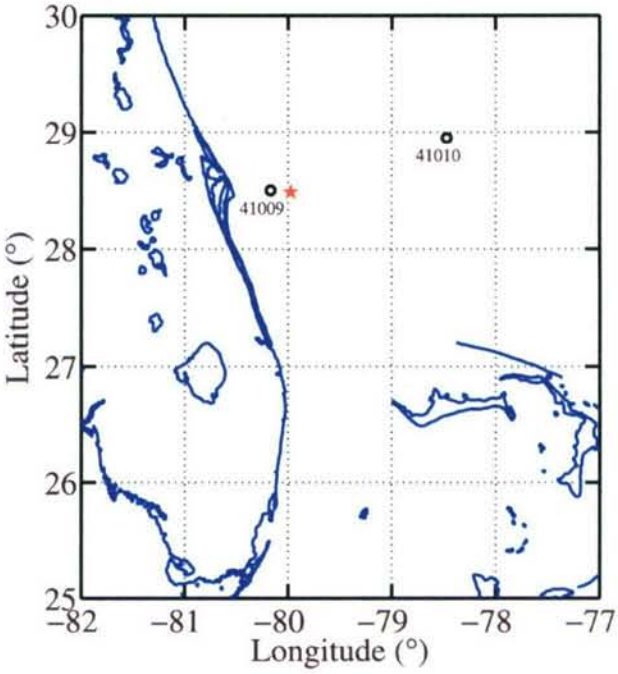

Figure 1. Map of the experimental site. Circles show the two NDBC buoys that provide the in situ wind and wave data used in this study. The star shows the location of DBI data.

which is about 15 km from the central location of the DBI data. The mean local water depth is 41.5 m. Buoy 41010 is located at 28.95°N 78.47°W, about 145 km from the DBI site, and the mean local water depth is 872.6 m. The data to be presented in this paper are collected from two flight passes on 13 March 2004. The starting time of the first pass (eastbound) is 00:30:22 UTC (marked with vertical dashed lines in Figure 2) and the duration of the data segment is 104 s. The second pass (westbound) occurred about 10 min later (starting time 00:40:18.6 UTC) with a duration of 106 s. The surface area of the DBI coverage in each flight pass is about 2.8 km × 10 km. The location of the DBI data is indicated by a star in Figure 1. The local water depth is about 100 m (estimated from the bathymetry map shown in Figure 2 of *Zantopp et al.* [1987]). Figure 2 shows the time series of wind speed, U_{10}, wind direction, θ_U, significant wave height, H_s, peak wave period, T_p, air temperature, T_a, and water temperature, T_w, recorded from the two buoys. As shown in the figure, a couple of high-wind events passed through the area in the week before data acquisition. The event on 10 to 11 March had sustained wind speeds between 10 and 12 m/s and lasted for about 16 hours. The weather system continued moving eastward and at the time of DBI experiment more than one day later, the significant wave height at the offshore buoy site (41010) is almost 5 m high although the wind speed dropped to below 5 m/s at both buoy locations. The wave height in the nearshore site (41009) is about one-half of the offshore magnitude. The peak wave periods reported by the two buoys are 14.29 s (41010) and 13.79 s (41009) at the time of DBI data. The water temperature at 41009 slowly increased during the

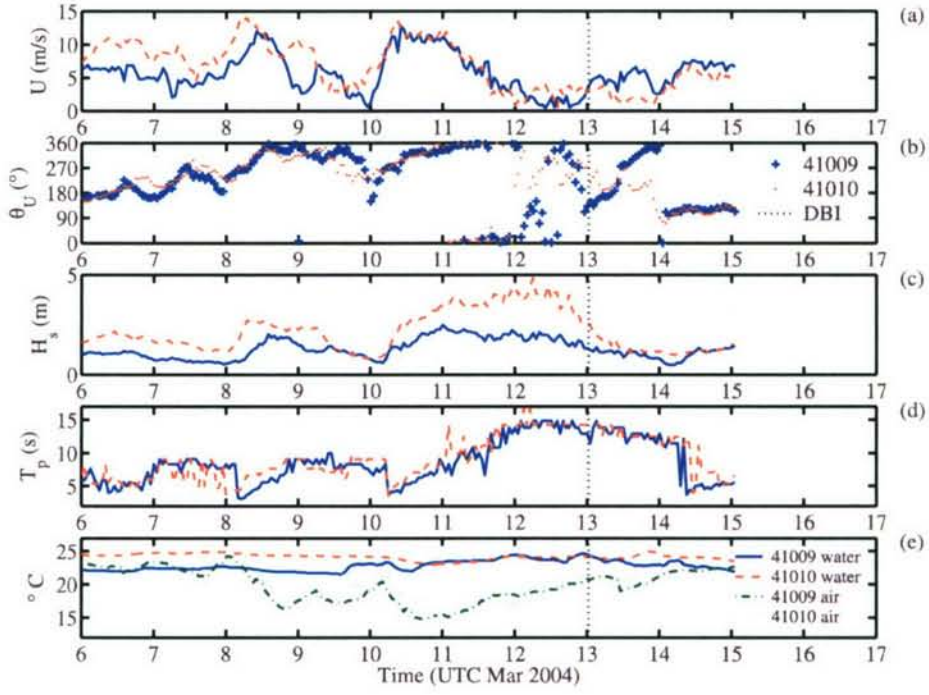

Figure 2. Time series showing (a) wind speed, (b) wind direction, (c) significant wave height, (d) peak wave period, and (e) air and water temperatures measured by buoys 41009 and 41010. The vertical dotted line in each panel indicates the time of DBI data acquisition.

week prior to the DBI data acquisition and reached the same temperature as that at 41010 on 10 March 2004, suggesting that the GS was moving shoreward during that period. Figure 3 shows the 2.55-day average sea surface temperature map provided by the Ocean Remote Sensing Group, Applied Physics Laboratory, Johns Hopkins University (http://srbdata.jhuapl.edu/d0043/avhrr/gs/averages/04mar/gs_04mar13_2016_multi.png). The locations of the two buoys are sketched on the map for reference; they are approximately on the two opposite ends of the thermal boundary depicting the GS.

2.2. Instrumentation

[8] A detailed analysis of the DBI design is given by *Frasier and Camps* [2001]. The DBI configurations used in the present experiment have been reported by *Farquharson et al.* [2004] and *Toporkov et al.* [2005]. A brief summary is given here. The DBI operates at C-band (5.3 GHz) and vertical polarization. It emits a 6.25-μs-long chirp signal with a 25-MHz bandwidth that provides a 6-m range resolution. The squint angles of the fore- and aft-looking antenna pairs are nominally +20° and −20°, respectively. The physical baseline in each pair is 1.23 m, only the fore-looking antenna in each pair transmits. The antennas point at a 70° incident angle in their squinted planes. The antenna patterns are broad in elevation (31°) and narrow in azimuth (7°). The aircraft speed is nominally 100 m/s and the altitude 600 m. The range of the incident angles of the image pixels is between 50° and 81°. Figure 4 shows the phase diagrams derived from the fore- and aft-looking InSAR pairs. Positive x is in the direction of the flight. The DBI is mounted on the port side of the aircraft and the projected range increases in the positive y direction. The top panel is the phase map derived from the aft-looking pair of antennas and the lower panel from the fore-looking pair. Image boundaries are tilted because of the antenna squints. Noisy, horizontally striped margins on left and right of each image lie outside the synthesized data range and contain no physical information. Significant change of the phase produced by the GS (on the right-hand half of the image) is clearly visible in both images. In the following discussions, the overlap region of the two images, marked by two vertical lines in each map, is further processed to obtain the ocean surface current.

[9] Data from the second pass are processed in a similar fashion. The common area (1.7 km × 7.8 km) of the two passes is then extracted for deriving the 3D solution of the three orthogonal surface velocity components. The procedure is described in the next section.

3. Data Processing

[10] The radial velocity components, u_1 and u_2, in the two squint directions are related to the phases, Φ_1 and Φ_2, by [*Frasier and Camps*, 2001; *Toporkov et al.*, 2005]

$$u_j = \frac{\Phi_j}{4\pi}\frac{\lambda}{B_e}V_p, \qquad j = 1, 2, \tag{1}$$

where λ is the radar wavelength, V_p the platform speed, and B_e the effective baseline, which is one-half of the physical along-track antenna separation because only one antenna in each pair is transmitting. With the present configuration, the range of current velocities without wraparound ambiguity is

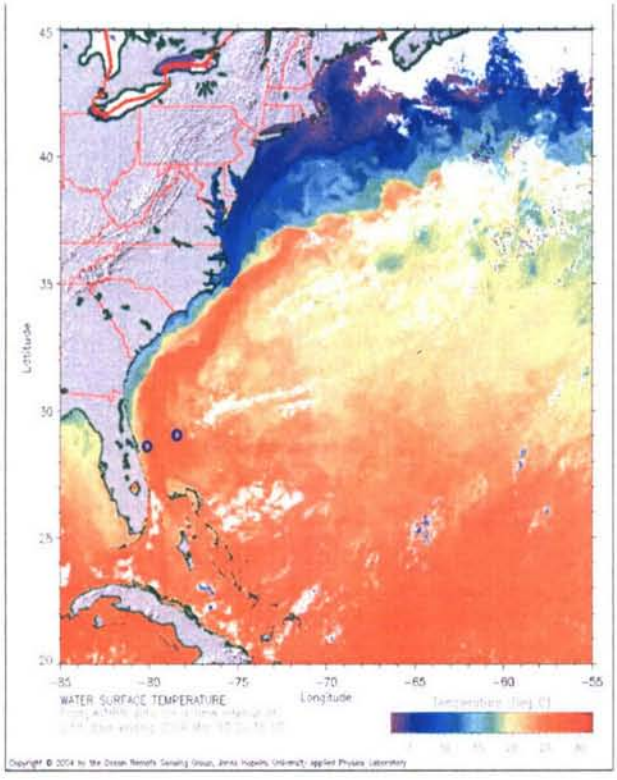

Figure 3. The average sea surface temperature on 13 March 2004 processed by the Remote Sensing Group, Applied Physics Laboratory, Johns Hopkins University (http://srbdata.jhuapl.edu/d0043/avhrr/gs/averages/04mar/gs_04mar13_2016_multi.png). The locations of the two buoys are sketched on the map for reference.

±2.30 m/s for the full range of the phase angles (±π). The raw processed phase data contain an arbitrary offset, which can be removed if there are fixed objects in the images for reference. This is not the case in the present situation. The aircraft makes repeated passes over the region; the time interval between two consecutive passes is about 600 s. Feature tracking is applied to estimate the velocities of several slick-like features in the radar scatter amplitude maps between two consecutive passes. The features in the inshore side of the GS usually maintain their coherent characteristics during the two passes and are easy to identify. Features inside the GS, however, are distorted beyond recognition between two passes and velocity estimates from feature tracking are only available for the inshore side of the GS front. The average velocity amplitude and direction of five identifiable features are 0.82 m/s and 103° (referenced to east). This average velocity is used in the data processing to determine the offset of the measured radar phase.

[11] Following the notations and geometry defined in Figure 5 (reproduced from Figure 1 of *Toporkov et al.* [2005]) and assuming that the current is confined to the horizontal plane, the surface velocity components can be calculated from the two radial components

$$v_x = \frac{u_1 \cos\theta_{s2} - u_2 \cos\theta_{s1}}{\sin(\theta_{s1} - \theta_{s2})}$$
$$v_y = \frac{u_2 \sin\theta_{s1} - u_1 \sin\theta_{s2}}{\sin(\theta_{s1} - \theta_{s2}) \sin\theta_i} \quad (2)$$

[12] The 2D solution (equation (2)) assumes that the vertical velocity component is negligible, that is, $v_z = 0$. This is a reasonable assumption for obtaining large-scale mean surface current and averaging over many pixels to

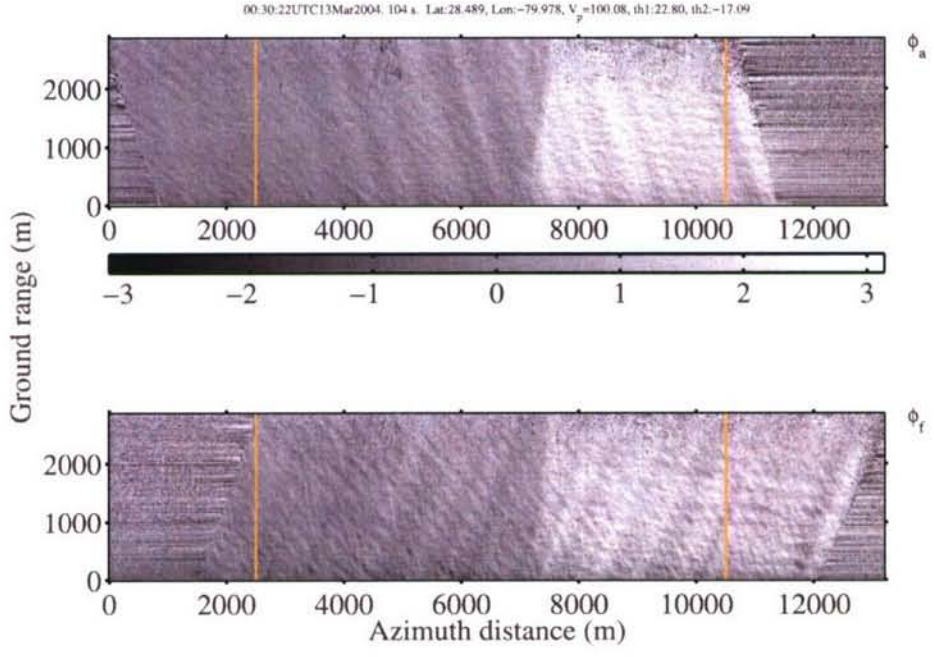

Figure 4. The phase maps of the DBI data, (top) aft-look, (bottom) fore-look. Vertical lines in the two maps show the overlap area used in the subsequent analysis.

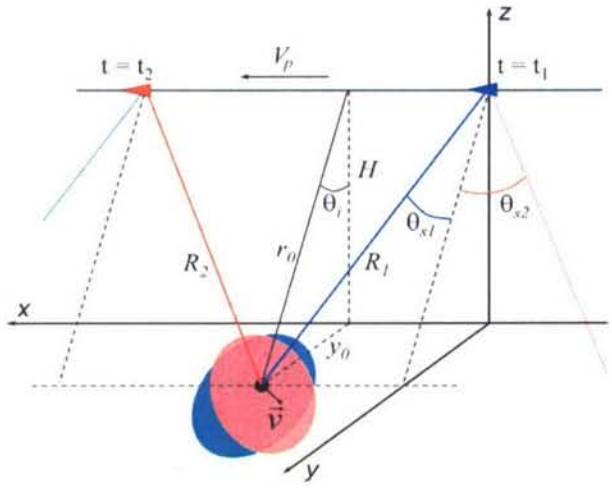

Figure 5. The system of coordinates and symbols used in this paper (Figure 1 of *Toporkov et al.* [2005]). The aircraft moves from right to left with velocity V_p, the antennas point toward the port side of the aircraft, one pair looking forward with a squint angle θ_{s1}, the other pair backward with a squint angle θ_{s2}. A common target on the ocean surface with velocity $\boldsymbol{v}$ is shown in the shaded ovals. The range is R_1 and R_2, respectively, for the fore- and aft-looking antenna pairs. The altitude of the aircraft is H and the incident angle θ_i.

suppress the surface wave effect is acceptable. For wave analysis, however, the assumption of $v_z = 0$ is no longer desirable. To derive all three orthogonal velocity components from the DBI measurements, we use the full formulation of the radial velocity,

$$u_j = v_x \sin\theta_{sj} + v_y \cos\theta_{sj} \sin\theta_{ij} - v_z \cos\theta_{sj} \cos\theta_{ij}. \quad (3)$$

where, $j = 1$ and 2 for the two beams in each pass. To combine the second flight pass over the same region to formulate three equations for the three unknowns in equation (3), the relative flight direction needs to be considered. Explicitly, combining two passes using the first pass as reference, with both beams from the first pass (incident angle $\theta_{i1} = \theta_{i2}$) and one beam from the second pass (flight direction α_3 relative to the first pass, incident angle θ_{i3}), the equation is

$$\begin{bmatrix} u_1 \\ u_2 \\ u_3 \end{bmatrix} = \begin{bmatrix} \sin\theta_{s1} & \cos\theta_{s1}\sin\theta_{i1} & -\cos\theta_{s1}\cos\theta_{i1} \\ \sin\theta_{s2} & \cos\theta_{s2}\sin\theta_{i2} & -\cos\theta_{s2}\cos\theta_{i2} \\ b_{31} & b_{32} & b_{33} \end{bmatrix} \begin{bmatrix} v_x \\ v_y \\ v_z \end{bmatrix}, \quad (4)$$

where $b_{31} = \sin\theta_{s3}\cos\alpha_3 - \cos\theta_{s3}\sin\theta_{i3}\sin\alpha_3$, $b_{32} = \sin\theta_{s3}\sin\alpha_3 - \cos\theta_{s3}\sin\theta_{i3}\cos\alpha_3$, and $b_{33} = \cos\theta_{s3}\sin\theta_{i3}$. Equation (4) can be written as $\boldsymbol{u} = \mathbf{B}\,\boldsymbol{v}$. The solutions of the three surface velocity components are

$$v_x = \frac{D_{B1}}{D_B}; \quad v_y = \frac{D_{B2}}{D_B}; \quad v_z = \frac{D_{B3}}{D_B}, \quad (5)$$

where D_B is the determinant of matrix $\mathbf{B}$, and D_{Bj} the determinant of the matrix formed by replacing the j-th column of $\mathbf{B}$ with vector $\boldsymbol{u}$. Additional discussions of the 3D solutions of InSAR measurements for both sidelooking (SLI) and dual-beam (DBI) systems, and a comparison of the 2D and 3D solutions of the SLI and DBI systems are given by P. A. Hwang et al. (unpublished manuscript, 2006).

[13] Figure 6 shows the three velocity components of the DBI measurements combining two passes. The mean flow of the GS system in this region is primarily northbound. From in situ current measurements, the daily average of the northbound velocity at the core of the GS is about 1.9 m/s (estimated from the contour map in Figure 13b of *Zantopp et al.* [1987]). The mean velocity of v_y displayed in Figure 6 (middle panel) represents an instantaneous snapshot of the surface current over a sizable region (the duration of the overlap data is about 78 s, the area of coverage about 1.7 km × 7.8 km), the maximum magnitude is about 2 m/s. A strong gradient in v_y is clearly shown. The velocity gradient near the GS front is about 1 m/s over a lateral distance of 500 m, corresponding to a strong velocity shear of 2×10^{-3} s^{-1}. The velocity contrast in v_x or v_z is much weaker and the boundary of the GS is barely discernable (top and bottom panels, Figure 6).

4. Wave Spectral Analysis

4.1. 2D Spectrum

[14] With velocity data like Figure 6, it is straightforward to compute the wavenumber spectrum of the surface waves using 2D fast Fourier transform (FFT). *Marom et al.* [1990, 1991] compare the wave properties derived from InSAR and in situ pressure gauge array in southern California. The wind speed is low (2 m/s) and the wave field swell-dominated. They show that the InSAR and buoy data are in very good agreement for waves propagating in the range direction and the quality of agreement deteriorates for waves traveling in the azimuth direction. Similar conclusion is reached by *Goldstein et al.* [1994]. The deteriorating agreement for wave components approaching azimuth direction (with wavelengths much longer than that affected by velocity bunching mechanism) is a fundamental problem of wave measurements by InSAR. The radial velocity is contributed by two velocity components in the vertical and ground range directions. An azimuth traveling wave gives no contribution to either component. Although in principal, this is taken into account in the $\sin\phi$ dependence of the transfer function between the spectra of surface velocity and surface elevation, the function has a second-order singularity behavior [$(k_x/k)^2 = 1/\sin^2\phi$, where k is the surface wavenumber and ϕ the wave propagation direction]. The noise in the system is greatly amplified for ϕ approaches zero when the transfer function is applied to convert the velocity spectrum to displacement spectrum. This singularity behavior is masked by the incident angle (θ) dependence in the transfer function between the radial velocity and the surface displacement spectra ($\sin^2\theta \sin^2\phi + \cos^2\theta)^{-1}$ [e.g., *Hasselmann and Hasselmann*, 1991]. When possible, it is much more straightforward using the

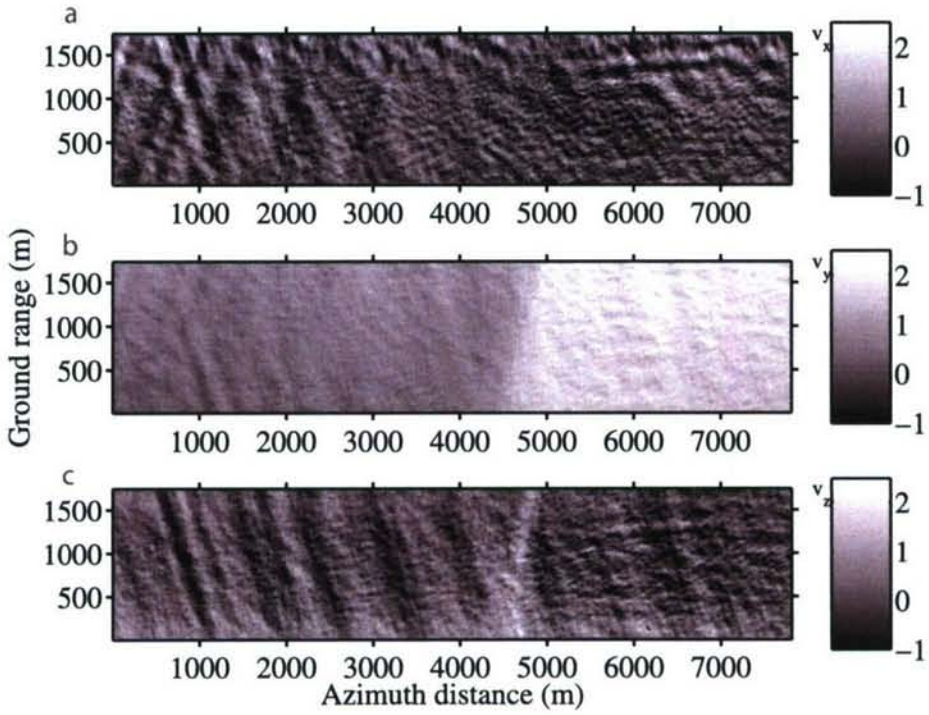

Figure 6. Maps showing the three orthogonal components of the surface velocity field, (a) v_x, (b) v_y, and (c) v_z, computed from combining two passes of the DBI measurements.

surface velocity components (instead of the radial velocity) for wave analysis, to be further explained in the following.

[15] Of the three components of the wave-induced orbital velocity, v_x, v_y and v_z, the vertical component is not dependent on the wave propagation direction, as shown below. For a given spectral wave component (denoted by subscript n), the surface displacement η_n, the stream function of the wave field φ_n, and the orbital velocity $\boldsymbol{v}_n = (v_{xn}, v_{yn}, v_{zn})$ are [e.g., *Phillips*, 1977]

$$\begin{aligned} \eta_n &= a_n \cos(k_n x - \omega_n t + \varepsilon_n), \\ \varphi_n &= \frac{\omega_n a_n \cosh k_n (z+h)}{k_n \sinh k_n h} \sin(k_n x - \omega_n t + \varepsilon_n), \\ v_n &= \nabla \varphi_n = \left(\frac{\partial \varphi_n}{\partial x}, \frac{\partial \varphi_n}{\partial y}, \frac{\partial \varphi_n}{\partial z} \right). \end{aligned} \tag{6}$$

where $\boldsymbol{k}$ is the wavenumber vector with modulus k, a wave amplitude, ω angular frequency, h water depth, t time and ε a random phase. For InSAR applications, $z = 0$ (for velocity at the surface) and t can be set to zero without loss of generality. Explicitly, the three components of the surface velocity are

$$\begin{aligned} v_{xn} &= \omega_n a_n \cos(k_n x + \varepsilon_n) \cos \phi_n \\ v_{yn} &= \omega_n a_n \cos(k_n x + \varepsilon_n) \sin \phi_n \\ v_{zn} &= \omega_n a_n \sin(k_n x + \varepsilon_n) \end{aligned} . \tag{7}$$

The surface displacement spectrum S_η can be calculated from the velocity spectrum S_v. The latter can be derived from the sum of the two spectra, S_{vx} and S_{vy}, computed from v_x and v_y, respectively, or from S_{vz} computed from v_z. That is, we can express the velocity components as the Fourier series

$$v_x = \sum_{n=1}^{\infty} v_{xn}; v_y = \sum_{n=1}^{\infty} v_{yn}; v_z = \sum_{n=1}^{\infty} v_{zn}. \tag{8}$$

The directional spectrum of a given wavenumber component, (k_n, ϕ_n), can be written as

$$\begin{aligned} S_{vx}(k_n, \phi_n) &= \cos^2 \phi_n S_v(k_n, \phi_n) \\ S_{vy}(k_n, \phi_n) &= \sin^2 \phi_n S_v(k_n, \phi_n) \\ S_{vz}(k_n, \phi_n) &= S_v(k_n, \phi_n) \end{aligned} . \tag{9}$$

The surface displacement spectrum is related to the velocity spectrum by

$$S_\eta(k) = \omega^{-2} S_v(k). \tag{10}$$

The wave angular frequency is related to wavenumber by the dispersion relation, $\omega^2 = gk \tanh kh$, where g is the gravitational acceleration.

[16] The region near the Gulf Stream boundary is dynamically active. Despite extensive efforts in the processing of motion compensation, considerable platform motions remain in the resulting velocity product. This is detectable visually, for example, as the low-frequency undulations in the phase and velocity maps (e.g., Figures 4 and 6). For

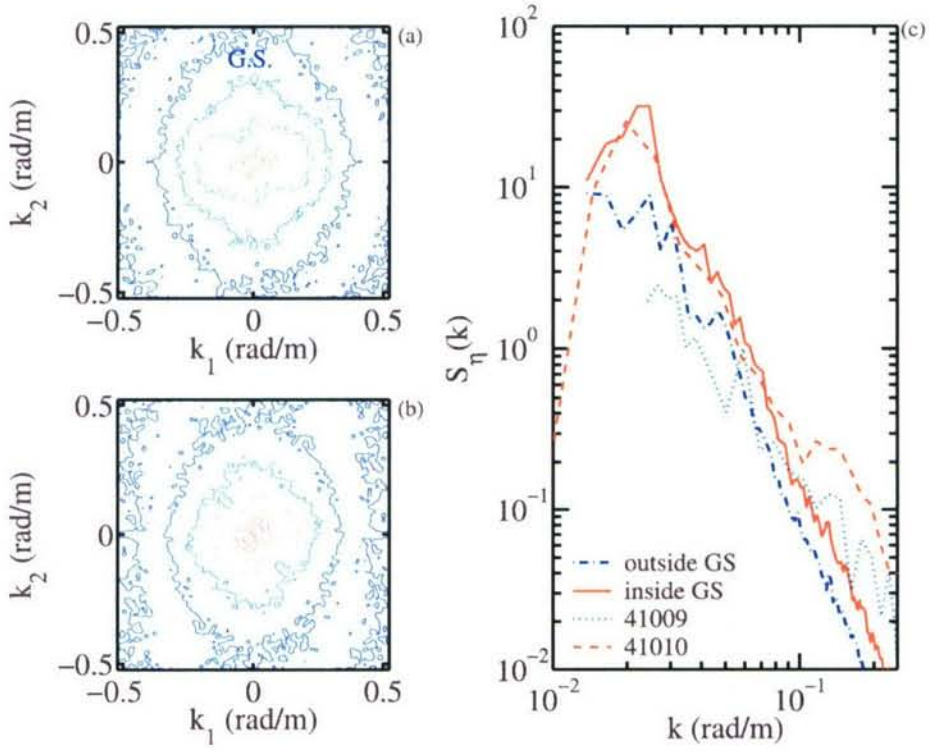

Figure 7. Comparison of the 2D wave spectra (a) inside and (b) outside the Gulf Stream, (c) 1D spectra from DBI and buoy measurements.

large-scale currents such as the GS or tidal flows through inlets, these residual errors of the platform motion can be reduced significantly by spatial smoothing. For the scale of surface gravity waves, the residual errors in the platform motion correction become a serious contamination to the wave signal. As analyzed in section 5, the signal to noise ratio (SNR) of the wave data (in terms of the variance ratio of waves and measurement uncertainties) is about two to six and represents a challenge in wave spectral analysis. An empirical scale decomposition (ESD) procedure similar to the empirical mode decomposition method of *Huang et al.* [1998, 1999] is developed to decompose the measured signal into several components, each with a narrow band of length scales. The spectral analysis is performed on each signal component to reduce the contamination of spectral signal in the wavelength band by the spectral leakage of longer-scale waves, which are usually of much higher spectral density – the wavenumber dropoff of a typical wind wave spectrum is $\boldsymbol{k}^{-3.5}$. More detail on the ESD is given in Appendix A2.

[17] Figures 7a and 7b display the 2D velocity spectra, $S_v(k_x, k_y)$, inside and outside GS calculated with v_z. As described in the last section, the wave field is the remnant from an earlier northerly event (Figure 2). This information can be used to resolve the180° ambiguity in the 2D spectra and it is reasonable to assume that the dominant directions of the wave components shown in Figure 7 are from the first quadrant. Significant wave height and peak wave period (H_s, T_p) at the time of radar data are (1.15 m, 13.8 s) recorded by Buoy 41009, and (2.60 m, 14.3 s) by Buoy 41010; the corresponding peak wavenumbers are 2.65×10^{-2} and 1.97×10^{-2} rad/m, respectively. The spectral peak wavenumbers derived from the DBI analysis are in reasonable agreement with the buoy measurements and will be further discussed in the next subsection describing the properties of the 1D wave spectrum (Figure 7c). Poorer resolution in the azimuth direction due to velocity bunching [e.g., *Alpers and Rufenach*, 1979; *Hasselmann et al.*, 1985] is clearly shown in the contours of the 2D spectra. For the present data set, the azimuth roll-off becomes serious at about $k_x = 0.25$ rad/m, which gives a Nyquist wavelength of 25 m and the effective resolution in the azimuth direction is 12.5 m. The nonlinearity of SAR measurements can be quantified by the dimensionless parameter $k_p u_r R/V_p$ [e.g., *Bao et al.*, 1999], where u_r is the magnitude of the wave orbital velocity. For the present data, $R \approx 2500$ m, $V_p \approx 100$ m/s, $k_p \approx 0.02$ rad/m, and $u_r \approx 0.22$ to 0.58 m/s for a swell of 14-s period and 0.6 to 1.3 m amplitude, the nonlinearity parameter is about 0.13 to 0.29 and the process of SAR image formation in the present data set is reasonably linear.

[18] Waves inside the GS are distinctively different from those outside the GS in three respects. (a) The spectral density level is considerably higher inside GS, by about a factor of two (Figure A2). (b) The directional distribution of the wave spectrum outside the GS is rotated counter-clockwise by about 20 to 30 degrees in comparison with that of the spectrum inside the GS. And (c) there is a conspicuous standing wave (cross-hatched) pattern in the dominant scale signal components in the GS side of the sharp current front (Figure A1).

[19] The directional difference of the two wave fields is consistent with that expected from wave-current interaction.

This can be illustrated by the wavenumber conservation equation (e.g., section 2.6 of *Phillips* [1977])

$$\frac{\partial k}{\partial t} + \nabla n = 0, \tag{11}$$

where n is the apparent frequency of the wave field, which is related to the intrinsic frequency, ω, by $n = \omega + \boldsymbol{k} \cdot \boldsymbol{U}$ and $\boldsymbol{U}$ the current vector. Assuming that the intrinsic frequency does not vary with space, the following equation describes the evolution of the wavenumber vector propagating through a current field

$$\frac{\partial k}{\partial t} = -\nabla(kU). \tag{12}$$

To apply this to the GS in the experimental location, the current field is simplified to $\boldsymbol{U} = (0, V)$, and $\partial/\partial y = 0$; thus (12) becomes

$$\begin{aligned} \frac{\partial k_1}{\partial t} &= -\frac{\partial (k_2 V)}{\partial x} \\ \frac{\partial k_2}{\partial t} &= 0 \end{aligned} \tag{13}$$

Figure 8 shows an example of the trajectories of waves with a southbound component going through a current field $V(x) = V_0 \exp[-(x/x_b)^q]$ with $q = 8$, scaling width $x_b = 80$ km, and maximum velocity $V_0 = 2$ m/s. (Note, even with $q = 8$ for the velocity profile, the maximum current shear is 7.4×10^{-5} s^{-1}, still much smaller than the observed value of 2×10^{-3} s^{-1} from the smoothed velocity map of v_y shown in Figure 6). In this plot, the reference direction of wave propagation is 0 degree in the opposite direction of current. The evolution of wave propagation is consistent with the 2D wavenumber spectra shown in Figure 7.

4.2. 1D Spectrum

[20] The DBI 2D wavenumber spectra can be integrated to yield 1D spectra to compare with the buoy measurements (Figure 7c). The buoy spectrum is in frequency domain and the following equation is used to convert the frequency spectrum to wavenumber spectrum,

$$S(k) = S(\omega)\frac{d\omega}{dk}. \tag{14}$$

As discussed in section 2 (Figure 2), the waves at the experimental site are dominated by the swell generated by an earlier northerly event. The wavenumbers at the spectral peaks at the two buoy sites are slightly different, 2.65×10^{-2} and 1.97×10^{-2} rad/m, respectively, for 41009 and 41010 (about 160 km apart). The difference in the spectral peak wavenumbers of the two buoy measurements can be explained by the refraction effect due to shoaling from deep to shallower water; the water depth is 873 m at buoy 41010 and 41.5 m at buoy 41009. Another factor is the Doppler frequency shift (not included in the frequency to wavenumber conversion here). For waves advected by a counter current with projected velocity of 1 m/s in the direction of wave propagation, the Doppler frequency shift introduces about 4 percent increase in the apparent frequency for $k =$ 0.02 rad/m. Using the energy flux conservation principle, $S_{11}(k)c_g(k) =$ constant, the shoaling effect (without external sources and sinks) can be quantified. Figure 9 shows the buoy and DBI spectra adjusted for shoaling refraction to the water depth of buoy 41009. The spectra computed from DBI are from two locations about 2.7 km apart (between the centers of the two squares used for spectral analysis) on the two sides of the sharp velocity front, 15 km from the inshore buoy (41009) and 145 km from the offshore buoy (41010). The refraction-adjusted spectral peak wavenumbers of DBI and buoy are all near 2.7×10^{-2} rad/m.

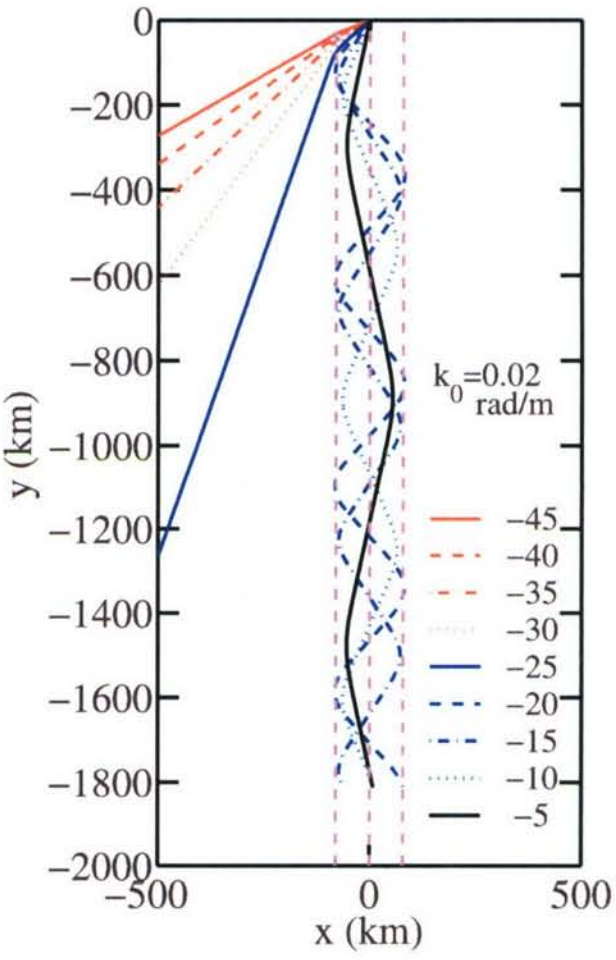

Figure 8. Numerical computations illustrating the wave trapping effect of the Gulf Stream wave guide, $k_0 = 2 \times 10^{-2}$ rad/m. The reference direction of wave propagation in the legend is 0 degree in the opposite direction of current.

[21] The most interesting part of this comparison is the difference of the two DBI spectra on the two sides of the velocity front. To the GS side, the DBI spectrum is essentially the same as that of buoy 41010, especially when the current modulation is also accounted for. Numerical computation of wave-current interaction shows a level of about 10 percent increase in wavenumber and wave variance inside the GS for wave components with initial (unperturbed) wavenumber of 0.02 to 0.03 rad/m (Appendix B). The wave spectrum of buoy 41010 adjusted for both shoaling refraction and wave-current modulation is

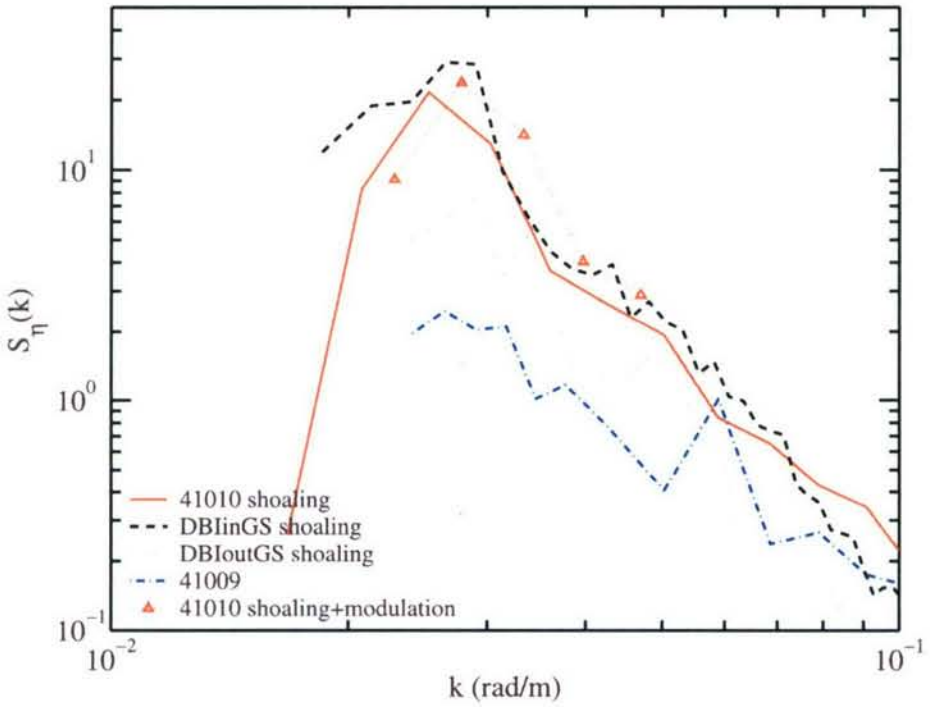

Figure 9. 1D spectra from DBI and buoy measurements adjusted for the effect of shoaling refraction using the depth of buoy 41009 as reference. The current modulation effect of the deep water (buoy 41010) spectrum is also shown.

sketched in Figure 9. It is fair to say that the difference between the DBI spectrum in the GS side of the velocity front and the spectrum at buoy 41010 is largely attributable to refraction and current modulation. This is not unexpected because the wave condition is dominated by the 14-s swell. The wave steepness of the swell is small, so dissipation by breaking or viscosity and generation by wind (5 m/s) do not modify this swell system over the 145-km distance between the two measurement sites. However, just a short distance away to the inshore side of the velocity front, the wave spectral density dropped drastically and a demarcation line can be drawn at the velocity front delineating two regions of very different surface wave properties.

5. Discussions

5.1. Gulf Stream Wave Guide

[22] Increased surface roughness at the current boundary is a frequently observed phenomenon. Modification of winds and waves by ocean current systems can also be observed from spaceborne altimeter measurements. For example, *Hwang* [2005] presented an analysis of the spatial variation of wind speeds and significant wave heights in the Yellow and East China Seas using six years data from the TOPEX/Poseidon (TP) output. The region has a distinctive monsoon pattern and the Kuroshio trajectory is stable due to bathymetric confinement. In winter months when waves are propagating obliquely against the Kuroshio, the spatial distribution of wave heights shows a clear modulation by the Kuroshio, with a peak enhancement of 25 to 50 percent of the wave variance observed. Three factors contributing to the wave enhancement are cited: increased (effective) wind speed in the Kuroshio domain leading to an increase in wave generation, hydrodynamic modulation due to wave-current interaction, and air-sea instability in the Kuroshio leading to an enhanced wave generation. The first factor can be calculated from the wind speed data available from the TP output. The second factor can be quantified by computation using the action density conservation equation. The result shows that each of the three factors contributes about one third to the total enhancement observed in the TP wave data.

[23] The factor-of-two increase of the wave variance (of the long swell) inside the GS in the present data set (Figure A2) is considerably higher than that expected from hydrodynamic modulation, calculated to be about 10 percent (unperturbed wavenumber, $k_0 = 2 \times 10^{-2}$ rad/m) and 12 percent ($k_0 = 3 \times 10^{-2}$ rad/m) for the GS. The computation of hydrodynamic modulation using the energy or action density conservation equation has been discussed in great detail elsewhere [e.g., *Longuet-Higgins and Stewart*, 1960; *Keller and Wright*, 1975; *Hughes*, 1978; *Phillips*, 1984; *Thompson and Gasparovic*, 1986; *Hwang and Shemdin*, 1990; *Hwang*, 1999, 2005] and a brief summary is given in Appendix B. As stated earlier, the waves are dominantly swell (wave period 14 s), thus effects of air-sea stability condition and wave-generation by local wind (of 5 m/s) can be ignored. A more likely mechanism contributing to the observed intensification of the wave field inside the GS is the "wave guide" effect produced by the strong velocity gradient at the GS boundary. With the right combinations of wave and current properties, (surface, internal or acoustic) waves can be trapped inside the GS. This effect occurs

when the change of k_1 following equation (13) is so large that k_1 changes sign (reversing the propagation direction). The formation of a wave guide by a shear current is a delicate combination of several parameters including the velocity shear, the current width, the wavelength and the wave propagation direction (so the wave guide formed by an ocean current is probably quite leaky). As shown in Figure 8 for $k_0 = 2 \times 10^{-2}$ rad/m, wave components inside the current that propagate at angles less than ±20° against the current are trapped. The spectral peak wavenumber of the wave field at the time of data collection is close to 2×10^{-2} rad/m and the source of swell is from northerly and northeasterly directions, the wave guide effect may be important in producing the large enhancement of waves inside the GS in the present data set.

[24] Another observation that provides further support of the wave trapping hypothesis is the standing wave (cross-hatched) pattern in the GS side of the velocity front. This feature is enhanced considerably through the ESD analysis (Appendix A). The cross-hatched pattern of the waveform in the decomposed components with length scales near the spectral peak wavelength on the GS side of the velocity front is suggestive of waves bouncing off the current front (see the velocity maps of f_{L2} and f_{L3} in the left panels of Figure A1). Based on the analysis presented in this paper, the Gulf Stream can be viewed as the Nature's hydraulic breakwater that protects the U.S. eastern seaboard. Without it, the severe waves reaching the coast from northeasterly storms may have been more energetic by a factor of two.

5.2. Measurement Uncertainty

[25] As mentioned earlier, there are considerable residual noises caused by the platform motion. Here the resolution issue is further investigated. *Frasier and Camps* [2001] and *Toporkov et al.* [2005] present an error analysis to quantify the accuracy of DBI velocity measurements based on the Cramer-Rao bound of the phase error variance [*Rodriguez and Martin*, 1992; *Rosen et al.*, 2000],

$$\sigma_{\Phi}^2 = \frac{1}{2N_L}\frac{1-\gamma^2}{\gamma^2}, \tag{15}$$

where N_L is the number of looks and γ the coherence parameter between the radar returns from the pair of antennas forming the InSAR. The variance of the error in the velocity measurements can be derived from (1) and (2) assuming that the phase noise in the fore- and aft-looking interferograms is uncorrelated [*Frasier and Camps*, 2001; *Toporkov et al.*, 2005]

$$\begin{aligned}\sigma_{vx}^2 &= \left(\frac{\lambda V_p}{4\pi B_e}\right)^2 \frac{\sigma_{\Phi 1}^2 \cos^2\theta_{s2} + \sigma_{\Phi 2}^2 \cos^2\theta_{s1}}{\sin^2(\theta_{s1}-\theta_{s2})} \\ \sigma_{vy}^2 &= \left(\frac{\lambda V_p}{4\pi B_e}\right)^2 \frac{\sigma_{\Phi 1}^2 \sin^2\theta_{s2} + \sigma_{\Phi 2}^2 \sin^2\theta_{s1}}{\sin^2(\theta_{s1}-\theta_{s2})\sin^2\theta_i}\end{aligned}. \tag{16}$$

With spatial smoothing of 20 × 20 pixels for the surface mean current, the accuracy of the velocity measurement is $\sigma_{vx} = 0.032$ m/s and $\sigma_{vy} = 0.013$ m/s in the present data set, comparable to that reported by *Toporkov et al.* [2005]. Without smoothing, $\sigma_{vx} = 0.33$ m/s and $\sigma_{vy} = 0.16$ m/s, which are very coarse for surface wave processing. For wave spectral analysis, a 3 × 3-pixel smoothing (2D running average) is applied, resulting in $\sigma_{vx} = 0.16$ m/s and $\sigma_{vy} = 0.069$ m/s. The root mean square amplitude of the wave-induced orbital velocity computed from the buoy-measured wave spectrum is 0.24 m/s at buoy 41009 and 0.41 m/s at buoy 41010. The signal to noise ratio (SNR) in terms of the velocity variance is 1.9 for waves near buoy 41009 and 5.5 near buoy 41010. While these figures are not detrimental, special care is needed in spectral analysis to extract the wave signal from the noisy background (Appendix A).

6. Summary

[26] A DBI employs two sets of InSAR to provide mapping of both horizontal velocity vectors of the ocean surface in a single flight pass. In an earlier study, it was shown that the resolved velocity fields over barrier islands follow the expected outflow pattern of tidal flows [*Toporkov et al.*, 2005]. In this paper, DBI data acquired in the vicinity of the GS boundary are analyzed. The 3D solution is derived to extract all three orthogonal surface current components from combining two flight passes over the same region. The retrieved mean current field (Figure 6) is in reasonable agreement with in situ measurements (section 3).

[27] Section 4 describes the wave spectra computed from the DBI data. The contamination by the platform motion is not fully removed in the present dataset due to the bumpy ride caused by the unstable stratification near the GS boundary. The SNR of the wave data is estimated to be about two to six and considerable care is needed for the spectral analysis. A new signal processing technique (ESD) is developed to improve the quality of wave spectral analysis (Appendix A). The result is in good agreement with in situ buoy output. The difference in the propagation directions of waves inside and outside the GS detected from the 2D wave spectra is consistent with the refraction effect expected from wave-current interaction. The wave variance inside GS is about twice that outside GS in the DBI data although the spatial separation is only about 2.7 km. The level of enhancement inside GS is considerably higher than that can be explained by hydrodynamic modulation. Generation of waves by local wind is not an important factor judging from the long wave period (14 s) and low wind speed (5 m/s); so is the air-sea stability effect and both factors can be ignored in this case. (Even when all three factors are important, earlier investigation indicates 25 to 50 percent wave variance enhancement by the Kuroshio using the TP data [*Hwang*, 2005].) A more likely explanation of the excessive wave enhancement in the present data set is that the GS can act as a wave guide and trap waves inside when the right combinations of wavelength, propagation direction, current width and shear level exist. Numerical computations suggest that the surface waves at the time of data acquisition may satisfy the selective conditions. The hypothesis is further supported by the appearance of standing wave (cross-hatched) pattern on the GS side of the velocity front, indicative of swell bouncing off the sharp velocity front as a result of wave trapping. The wave analysis of DBI measurements shows that the Gulf Stream is Nature's hydraulic breakwater protecting the U.S. eastern

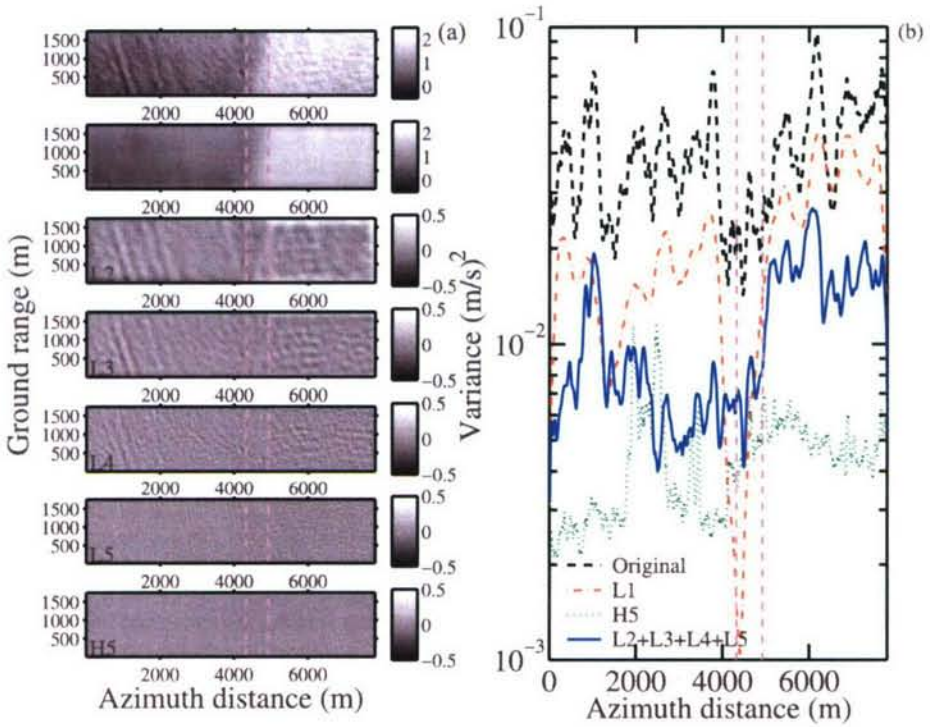

Figure A1. (a) An example showing the ESD process. The velocity maps shown are the original data ($f(x)$), five longer scale components ($f_{L1}(x)$, $f_{L2}(x)$, ..., $f_{L5}(x)$), and the short scale component ($f_{H5}(x)$). Notice the standing wave (cross-hatched) pattern in f_{L2} and f_{L3} on the GS side of the velocity front. (b) The corresponding column-by-column variance of the original signal and decomposed components shown to the left. The sum of the variance of scale components f_{L2} to f_{L5} (dominated by the swell signals) is added as one curve to simplify the figure. Contamination from residual platform motion is quite severe for all components in the neighborhood of azimuth distance ~1000 m.

seaboard. It reduces by half the intensity of severe waves reaching the coast from northeasterly storms.

Appendix A: Additional Notes on Data Analysis

A1. Combining Flight Tracks With Time Lags

[28] When combining InSAR measurements from different flight passes, the current fields on the ocean surface are obviously taken from different times. Assuming that the spectra of wave and current fields are quasi-stationary (ergodic), the orbital velocity field of a give spectral component for the i-th pass can be written as

$$\begin{aligned} v_x &= \omega a \cos(kx - \delta_i)\cos\theta \\ v_y &= \omega a \cos(kx - \delta_i)\sin\theta \\ v_z &= \omega a \sin(kx - \delta_i) \end{aligned}, \tag{A1}$$

where δ_i is the phase lag (ωt_i). In combining two passes, say $\delta_1 = 0$, $\delta_2 = \delta$, we can introduce a new time reference with an offset $\Delta t = \pm\delta/2\omega$, and the velocity field in the two passes can be written as

$$\begin{aligned} v_x &= \omega a \cos(kx - \omega t' - \delta/2)\cos\theta \\ v_y &= \omega a \cos(kx - \omega t' - \delta/2)\sin\theta \\ v_z &= \omega a \sin(kx - \omega t' - \delta/2) \end{aligned}, \tag{A2}$$

that is, the time lag introduces a phase lag in the combined wave-induced flow field and does not change the spectrum. This analysis can be extended to combinations with more than two flight passes.

[29] The above discussion is applied to a Fourier spectral component of the surface current field. For different Fourier components, the phase lags are different but the spectrum is not affected because of the assumption of random phase lags inherent in the spectral analysis. In other word, the resulting current field is an equivalent realization produced by the expected current spectrum. The radial velocity measured by the radar at a given location on the water surface is a linear combination of the three orthogonal components of the surface velocity at that location (equation (3)), therefore, the field of radial velocity from combining different flight tracks is also an equivalent realization produced by the expected current spectrum. In the present data set, it is a good assumption that the swell condition remains ergodic during the 10-minute period between two flight passes.

A2. Empirical Scale Decomposition

[30] One of the difficult problems in airborne data processing is the low SNR because the complete removal of platform motion is not easy. This problem also exists in signals that contain many scales, for example, short wind-generated waves in the radar Bragg resonance scale embedded in longer wind waves and swell. In addition, due to

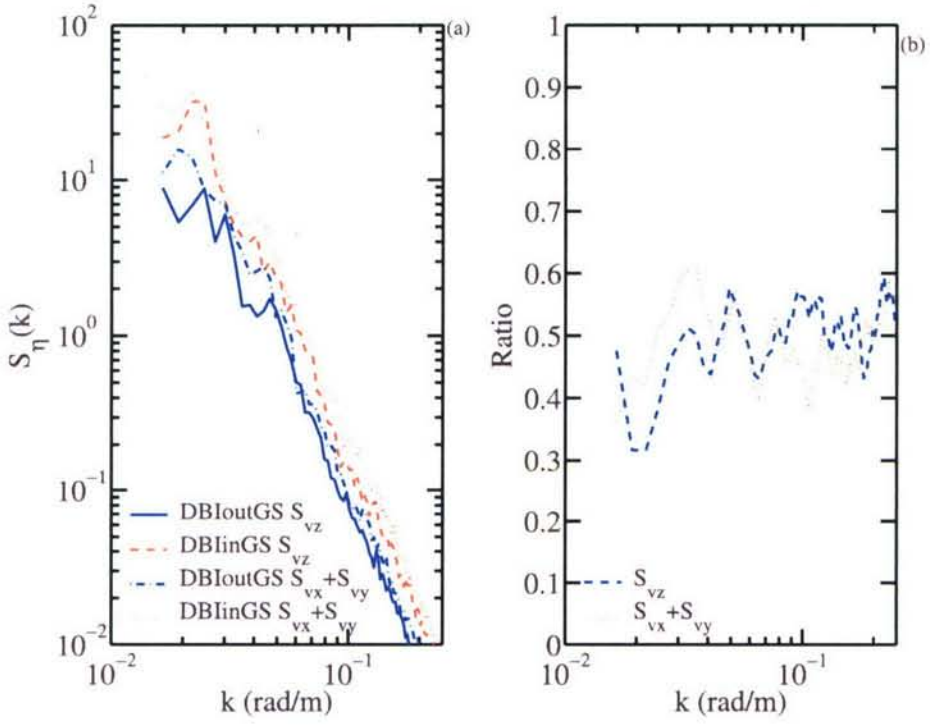

Figure A2. (a) Comparison of the surface wave spectrum computed from v_z, denoted as S_{vz} in the legend, and the sum of the spectra computed from v_x and v_y, denoted as $S_{vx} + S_{vy}$ in the legend. (b) The ratio between the wave spectra outside and inside the GS.

hydrodynamic modulation, the distribution of short waves on longer waves or in areas with current shears is no longer homogeneous or isotropic, which is an important assumption in Fourier spectral analysis. As a result of such "riding wave" problem, the spectral signature of short waves is frequently overwhelmed by the spectral leakage from longer scale wave components because the spectral density distribution of wind waves scales roughly with $\boldsymbol{k}^{-3.5}$. *Huang et al.* [1998, 1999] pioneered an empirical mode decomposition (EMD) designed to reposition the riding waves at the mean water level. The main idea is to find the trend that can represent the mean local average so that riding waves can be identified. The EMD method uses the point-by-point average of the signal envelopes for the local mean. The difference between the original signal and the local mean represents a mode of the signal. The local mean may also contain riding waves, and the mode decomposition process continues until no riding waves exist in the local mean component. The associated spectral analysis (Hilbert-Huang Transformation – HHT) provides superior spatial (temporal) and wavenumber (frequency) resolution for nonstationary (or inhomogeneous in space) and nonlinear data. The HHT spectrum also results in a considerably different interpretation of nonlinearity (frequency modulation instead of harmonic generation) [*Hwang et al.*, 2003]. In the EMD method, the length scales of each mode are usually mixed but the bandwidth of each mode is generally much narrower than that of the original signal. The EMD can be extended to 2D processing by decomposing the data in 1D line-by-line (Huang, personal communication).

[31] Here 2D digital filter (filter2 function in MATLAB) is used for signal decomposition of the 3D data such as the velocity maps in this paper. Because digital filter specifies length scales for high- and low-pass operation, the process is called empirical scale decomposition (ESD). Basically, a signal $f(x)$ is decomposed sequentially into a low-pass and a high-pass component,

$$\begin{aligned} f(x) &= f_{L1}(x) + f_{H1}(x) \\ f_{H1}(x) &= f_{L2}(x) + f_{H2}(x) \\ f_{H2}(x) &= f_{L3}(x) + f_{H3}(x) \\ &\cdots \\ f_{HN-1}(x) &= f_{LN}(x) + f_{HN}(x), \end{aligned} \tag{A3}$$

which can also be written as

$$f(x) = f_{L1}(x) + f_{L2}(x) + f_{L3}(x) + \ldots + f_{LN}(x) + f_{HN}(x). \tag{A4}$$

The f_{L1} component thus represents the large-scale trend in the data and f_{HN} may be the high-frequency noise or more isotropic short waves. Figure A1 shows an example of the ESD analysis of the v_y signal of the DBI data. The maps plotted on the left-hand side from top to bottom are f, f_{L1}, f_{L2}, f_{L3}, f_{L4}, f_{L5}, and f_{H5}, in the notation of this appendix. The scale for the sequential filtering is empirically set at $72\Delta x$, $36\Delta x$, $24\Delta x$, $12\Delta x$ and $6\Delta x$, where $\Delta x = 6$ m, therefore, the

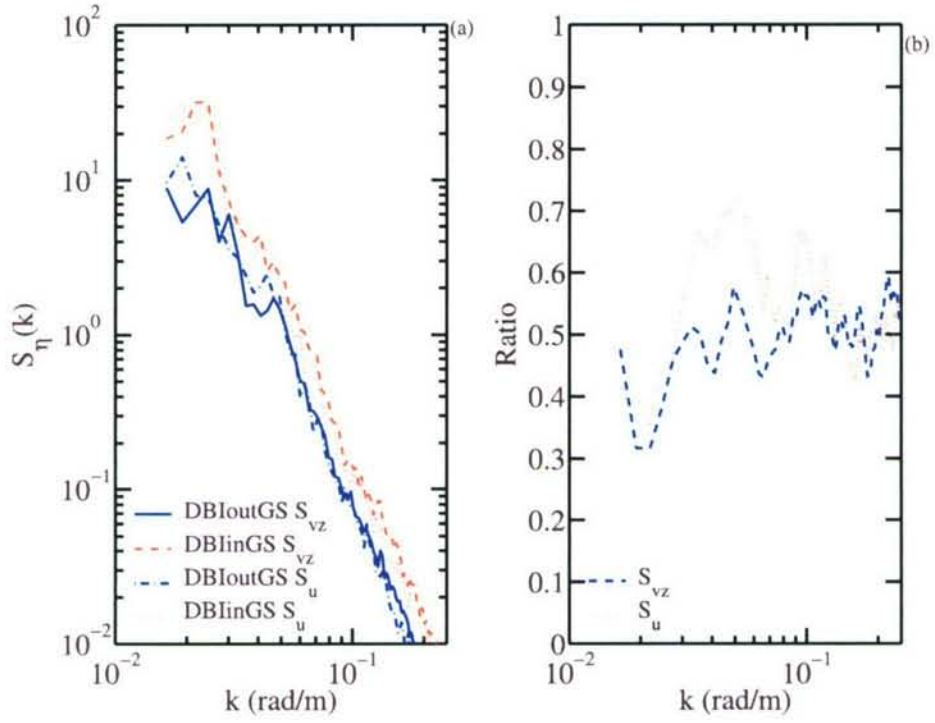

Figure A3. (a) Comparison of the surface wave spectrum computed from v_z, denoted as S_{vz} in the legend, and the radial velocity, u, denoted as S_u in the legend. (b) The ratio between the wave spectra outside and inside the GS.

wavelength of each filter sequence is 432, 216, 144, 72 and 36 m. It is quite interesting to see that the cross-hatched patterns of f_{L2} and f_{L3} in the GS side of the current front are enhanced considerably through this decomposition process. The choice of the upper and lower filter wavelengths (432 and 36 m) is based on the consideration of the wave conditions of the present data set that the dominant swell wavelength is about 300 m and the azimuth degrading becomes serious at about 25 m wavelength.

[32] The column-by-column variance of the corresponding signal components is plotted on the right-hand panel. We expect that the components f_{L2}, f_{L3}, f_{L4}, and f_{L5} contain most of the swell signal and f_{H5} the locally-generated wind waves. Notice that the variance of the wave signals is quite small compared to that of the f_{L1} component, which is contributed by a mixture of large-scale mean current variations, residual platform motion and spatial inhomogeneities. The spectra shown in Figure 7 are the sum of the individual spectra computed from the five wave signal components (f_{L2}, f_{L3}, f_{L4}, f_{L5}, and f_{H5}) using v_z. In the spectral processing of each decomposed signal component, a small area ($256\Delta x \times 256\Delta x$) is extracted from each side of the velocity front. Detrending of the area by high-pass with $72\Delta x$ (432 m) as the filter length parameter is performed prior to 2D FFT.

[33] As discussed in section 4, the 2D wave spectrum can also be calculated from the sum of the spectra of v_x and v_y. Figure A2 compares the wave spectra computed from these two approaches (spectrum of v_z and the sum of spectra of v_x and v_y). The results are comparable especially in the contrast (ratio) of wave properties on the two sides of the current front (Figure A2b).

[34] The wave spectrum can also be calculated from the radial velocity directly. The transfer function relating the radial velocity to the surface elevation is [*Hasselmann and Hasselmann*, 1991]

$$T_k^r = -\omega\left(\sin\theta_i \frac{k_l}{k} + i\cos\theta_i\right), \tag{A5}$$

where θ_i is the average incident angle and k_l the component of wavenumber vector in the radar look direction. Figure A3 compares the spectra derived from the vertical orbital velocity and the radial velocity. Very good agreement is found in this swell-dominant data set.

Appendix B: Wave-Current Interaction

[35] The wave action density conservation equation can be used to quantify the modulation of surface waves by surface currents [e.g., *Keller and Wright*, 1975; *Hughes*, 1978; *Phillips*, 1984; *Thompson and Gasparovic*, 1986; *Hwang and Shemdin*, 1990; *Hwang*, 1999, 2005],

$$\frac{dN}{dt} = \frac{\partial N}{\partial t} + \frac{\partial N}{\partial \vec{x}}\frac{\partial \vec{x}}{\partial t} + \frac{\partial N}{\partial \vec{k}}\frac{\partial \vec{k}}{\partial t} = \sum Q_i, \tag{B1}$$

where N is the wave action, t time, $\vec{x} = (x, y)$ the space vector, $\vec{k} = (k_1, k_2)$ the wavenumber vector, and Q_i source

terms (the notations used in this appendix are slightly different from those used in the main text). The partial differential equation (B1) can be transformed into a system of ordinary differential equations,

$$\frac{dN}{dt} = \sum Q_i, \tag{B2}$$

$$\frac{d\vec{x}}{dt} = \vec{c}_g + \vec{U}, \tag{B3}$$

$$\frac{d\vec{k}}{dt} = -k_1 \nabla U - k_2 \nabla V, \tag{B4}$$

where $\vec{c}_g$ is the group velocity, and $\vec{U} = (U, V)$ the current vector. Equations (B2) (B3)–(B4) can be solved by the method of characteristics [e.g., *Hughes*, 1978; *Hwang and Shemdin*, 1990] and equation (B4) is identically the conservation of wavenumber, equation (11) in the main text. Because the wavelengths investigated here are relatively long, the magnitudes of the source functions of wind input and breaking dissipation – based on *Plant* [1980] or *Hughes* [1978] formulations, for example – are very small. Numerical experiments with or without source functions did not produce significant differences in the computational results. In the present paper, all computations are based on zero external source terms. The only mechanism contributing to the modulation is the spatial variation of the surface velocity in the GS. For the modulation computation, the surface velocity is assumed to follow a 1D bell-shaped profile,

$$V(x) = V_0 \exp\left[-\left(\frac{x}{x_b}\right)^q\right], \tag{B5}$$

where V_0 is the peak current velocity at the axis (2 m/s assumed), and x_b a scale width of the current (80 km assumed). Numerical computations show that the level of wave variance enhancement attributable to hydrodynamic modulation is about 10 to 12 percent for waves with initial (unperturbed) wavenumbers from 0.02 to 0.03 rad/m. The wavenumber inside GS also increases by a similar proportion.

[36] **Acknowledgments.** This work is sponsored by the Office of Naval Research (NRL PE 61153 and 62435) and a grant of computer time from DOD High Performance Computing Modernization Program at the Naval Research Laboratory Distributed Center, the U.S. Army Engineer Research and Development Center, and the U.S. Army Space and Missile Defense Command Advanced Research Center. NRL contribution JA/7330–06-6082.

References

Alpers, W., and K. Hasselmann (1978), The two-frequency microwave technique for measuring ocean-wave spectra from an airplane or satellite, *Boundary Layer Meteorol.*, *13*, 215–230.

Alpers, W. R., and C. L. Rufenach (1979), The effect of orbital motions on synthetic aperture radar imagery of ocean waves, *IEEE Trans. Antennas Propag.*, *AP-27*, 685–690.

Bao, M., W. Alpers, and C. Brüning (1999), A new nonlinear integral transform relating ocean wave spectra to phase image spectra of an along-track interferometric synthetic aperture radar, *IEEE Trans. Geosci. Remote Sens.*, *37*, 461–466.

Farquharson, G., W. J. Junek, R. Ramanathan, S. J. Frasier, R. Tessier, D. J. McLaughlin, M. A. Sletten, and J. V. Toporkov (2004), A pod-based dual-beam SAR, *IEEE Geosci. Remote Sens. Lett.*, *1*, 62–65.

Frasier, S. J., and A. J. Camps (2001), Dual-beam interferometry for ocean surface current vector mapping, *IEEE Trans. Geosci. Remote Sens.*, *39*, 401–414.

Goldstein, R. M., and H. A. Zebker (1987), Interferometric radar measurement of ocean surface currents, *Nature*, *328*, 707–709.

Goldstein, R. M., T. P. Barnett, and H. A. Zebker (1989), Remote sensing of ocean currents, *Science*, *246*, 1282–1285.

Goldstein, R. M., F. Li, J. Smith, R. Pinkel, and T. P. Barnett (1994), Remote sensing of ocean waves: The surface wave process program experiment, *J. Geophys. Res.*, *99*, 7945–7950.

Graber, H. C., D. R. Thompson, and R. E. Carande (1996), Ocean surface features and currents measured with synthetic aperture radar interferometry and HF radar, *J. Geophys. Res.*, *101*, 25,813–25,832.

Hasselmann, K., and S. Hasselmann (1991), On the nonlinear mapping of an ocean wave spectrum into a synthetic aperture radar image spectrum and its inversion, *J. Geophys. Res.*, *96*, 10,713–10,729.

Hasselmann, K., R. K. Raney, W. J. Plant, W. Alpers, R. A. Shuchman, D. R. Lyzenga, C. L. Rufenach, and M. J. Tucker (1985), Theory of synthetic aperture radar ocean imaging: A MARSEN view, *J. Geophys. Res.*, *90*, 4659–4686.

He, Y., and W. Alpers (2003), On the nonlinear integral transform of an ocean wave spectrum into an along-track interferometric synthetic aperture radar image spectrum, *J. Geophys. Res.*, *108*(C6), 3205, doi:10.1029/2002JC001560.

Huang, N. E., Z. Shen, S. R. Long, M. C. Wu, H. H. Shih, Q. Zheng, N. C. Yuen, C. C. Tung, and H. H. Liu (1998), The empirical mode decomposition and the Hilbert spectrum for nonlinear and nonstationary time series analysis, *Proc. R. Soc. London*, *454A*, 903–995.

Huang, N. E., Z. Shen, and S. R. Long (1999), A new view of nonlinear water waves: The Hilbert spectrum, *Annu. Rev. Fluid. Mech.*, *31*, 417–457.

Hughes, B. A. (1978), The effect of internal waves on surface wind waves: 2. Theoretical analysis, *J. Geophys. Res.*, *83*, 455–465.

Hwang, P. A. (1999), Microstructure of ocean surface roughness: A study of spatial measurement and laboratory investigation of modulation analysis, *J. Atmos. Oceanic Technol.*, *16*, 1619–1629.

Hwang, P. A. (2005), Altimeter measurements of the wind and wave modulation by the Kuroshio in the Yellow and East China Seas, *J. Oceanogr.*, *61*, 987–993.

Hwang, P. A., and O. H. Shemdin (1990), Modulation of short waves by surface currents: A numerical solution, *J. Geophys. Res.*, *95*, 16,311–16,318.

Hwang, P. A., N. E. Huang, and D. W. Wang (2003), A note on analyzing nonlinear and nonstationary ocean wave data, *Appl. Ocean Res.*, *25*, 187–193.

Keller, W. C., and J. W. Wright (1975), Microwave scattering and the straining of wind-generated waves, *Radio Sci.*, *10*, 135–147.

Longuet-Higgins, M. S., and R. W. Stewart (1960), Changes in the form of short gravity waves on long waves and tidal currents, *J. Fluid. Mech.*, *8*, 565–583.

Marom, M., R. M. Goldstein, E. B. Thornton, and L. Shemer (1990), Remote sensing of ocean wave spectra by interferometric synthetic aperture radar, *Nature*, *345*, 793–795.

Marom, M., L. Shemer, and E. B. Thornton (1991), Energy density directional spectra of a nearshore wave field measured by interferometric synthetic aperture radar, *J. Geophys. Res.*, *96*, 22,125–22,134.

Phillips, O. M. (1977), *The Dynamics of the Upper Ocean*, 2nd ed., 336 pp., Cambridge Univ. Press, New York.

Phillips, O. M. (1984), On the response of short ocean wave components at a fixed wavenumber to ocean current variations, *J. Phys. Oceanogr.*, *14*, 1425–1433.

Plant, W. J. (1980), On the steady-state energy balance of short gravity wave systems, *J. Phys. Oceanogr.*, *10*, 1340–1352.

Rodriguez, E., and J. M. Martin (1992), Theory and design of interferometric synthetic aperture radars, *Proc. Inst. Electr. Eng. F*, *139*, 147–159.

Rodriguez, E., D. Imel, and B. Houshmand (1995), Two-dimensional surface wave currents using vector along-track interferometry, paper presented at PIERS'95 Conference, Seattle, Wash.

Rosen, P. A., S. Hensley, I. R. Joughin, F. K. Li, S. N. Madsen, E. Rodriguez, and R. M. Goldstein (2000), Synthetic aperture radar interferometry, *Proc. IEEE*, *88*, 333–382.

Shemer, L., M. Marom, and D. Markman (1993), Estimates of currents in the nearshore ocean region using interferometric synthetic aperture radar, *J. Geophys. Res.*, *98*, 7001–7010.

Thompson, D. R., and R. F. Gasparovic (1986), Intensity modulation in SAR images of internal waves, *Nature*, *320*, 345–348.

Toporkov, J., D. Perkovic, G. Farquharson, M. A. Sletten, and S. J. Frasier (2005), Sea surface velocity vector retrieval using dual-beam interferometry: First demonstration, *IEEE Trans. Geosci. Remote Sens.*, *43*, 2494–2502.

Vachon, P. W., J. W. M. Campbell, A. L. Gray, and F. W. Dobson (1999), Validation of along-track interferometric SAR measurements of ocean surface waves, *IEEE Trans. Geosci. Remote Sens.*, *37*, 150–162.

Zantopp, R. J., K. D. Leaman, and T. N. Lee (1987), Florida Current meanders: A close look in June–July 1984, *J. Phys. Oceanogr.*, *17*, 584–593.

P. A. Hwang, D. Lamb, M. A. Sletten, and J. V. Toporkov, Naval Research Laboratory, 4555 Overlook Ave., SW, Washington, DC 20375, USA. (phwang@ccs.nrl.navy.mil)

D. Perkovic, Microwave Remote Sensing Laboratory, University of Massachusetts, Amherst, MA 01003, USA.